ISPRS Annals of the Photogrammetry, Remote Sensing and Spatial Information Sciences, Volume XI-1-2026
XXV ISPRS Congress 2026 “From Imagery to Understanding”, Commission I, 4–11 July 2026, Toronto, Canada

Atmospheric correction of aerial imagery using satellite-derived reflectance data

Alexane Nghien, Manchun Lei, Mathieu Brédif

Univ Gustave Eiffel, Géodata Paris, IGN, LASTIG, F-77454 Marne-la-Vallée, France - firstname.lastname@ign.fr

Keywords: Atmospheric correction, Surface reflectance, Pseudo-Invariant Features, Sentinel-2, Airborne sensor

Abstract

Atmospheric correction of large-scale aerial imagery remains a major challenge, mainly due to the difficulty of accurately estimating atmospheric parameters from the images. Physical atmospheric correction methods are based on radiative transfer models, which require knowledge of atmospheric parameters at the exact time of acquisition, such as aerosol content. This study proposes a novel atmospheric correction approach based on satellite-derived Surface Reflectance (SR). The method is a semi-empirical linear correction model that leverages Pseudo-Invariant Features (PIFs) as reference points. By using the satellite-derived SR of these invariant targets as reference values, atmospheric correction of aerial images can be achieved without aerosol measurements. Experimental results show that, the proposed method achieves performance comparable to radiative transfer model approach when accurate atmospheric parameters are available, and provides more reliable corrections when such parameters are uncertain or unavailable. Also, the proposed approach reduces radiometric calibration differences between airborne and satellite images.

1. Introduction

Atmospheric correction is a crucial pre-processing for removing atmospheric effects in remote sensing data in order to retrieve the SR. Because most quantitative remote sensing applications rely on SR (Liang, 2005), accurate atmospheric correction is essential. Moreover, it enables reliable multi–temporal analysis (Hadjimitsis et al., 2010) and improves land cover classification accuracy (Rumora et al., 2020). A number of well established atmospheric correction methods have been developed for multispectral satellite sensors and are now routinely used in operational processing chains (Kaufman and Sendra, 1988, Vermote et al., 1997a, Hagolle et al., 2017).

In addition to satellite imagery, aerial photogrammetric images used for mapping and 3D modelling, provide very high spatial resolution and high geometric accuracy. When radiometrically calibrated and atmospherically corrected, aerial photogrammetric images can provide reliable SR data suitable for quantitative remote sensing applications (Honkavaara et al., 2009). However, these images are still not widely used for this purpose because their atmospheric correction remains an open issue.

A main problem is that these images do not have specific spectral bands that allow estimating atmospheric parameters from the images themselves. In the absence of such information, atmospheric correction is often performed using simplified empirical approaches such as the Empirical Line (EL) method (Smith and Milton, 1999) based on in-situ ground truth measurements (Collings et al., 2011, Berra et al., 2019, Guo et al., 2019, Jiang et al., 2022). Nevertheless, when a large number of aerial images acquired at different times cover a wide area, in-situ measurements become difficult or even impossible. In such cases, using satellite-derived SR data offers a promising alternative for atmospheric parameter estimation and correction.

This study aims to develop an atmospheric correction method for aerial imagery that does not rely on accurate atmospheric parameter estimation or in-situ measurements, enabling its application to large-scale datasets. Our approach is based on two main steps: (i) the extraction of radiometrically invariant features from images as proxy ground truth, and (ii) the use of well-calibrated multispectral satellite-derived SR as reference data, serving as an alternative to in-situ measurements.

2. Related work

Retrieving SR is a crucial exercise for various physical, biophysical and biological applications (Scotford and Miller, 2005). Atmospheric radiative transfer models (RTMs) such as SMAC (Rahman and Dedieu, 1994) and 6S (Vermote et al., 1997b), perform atmospheric modeling based on Aerosol Optical Thickness (AOT) obtained at the time of acquisition. With in-situ measures (Sharma et al., 2009), RTMs can be efficient in retrieving SR. In situation where in-situ ground measures are not provided, the satellite-derived AOT can provide sufficient information to parameterize RTMs for surface albedo retrieval (Zhao et al., 2001). However, AOT estimation methods add an error to the atmospheric correction (Hagolle et al., 2008), as it varies both temporally and spatially. All methods rely on the correct estimation of atmospheric parameters.

Numerous semi-empirical methods have been developed to derive SR from at-sensor reflectance (Collings et al., 2011). Relative Radiometric Normalization (RRN) techniques (Elvidge et al., 1995) are commonly employed to achieve radiometric harmonization between two images acquired by the same sensor. These approaches assume a semi-empirical relationship between ground-level and sensor-level radiometry, as in the EL method (Smith and Milton, 1999), along the viewing direction. Two main categories of RRN methods (Moghimi et al., 2021) can be distinguished: dense approaches, which use all available pixels for normalization (Volpi et al., 2015), and sparse approaches, which rely on radiometrically stable and invariant features.

PIFs (Schott et al., 1988) play a crucial role in achieving accurate normalization. They represent features where the radiometric values acquired by the sensors do not change among one or several criteria (time, atmospheric variations, viewing angle...). Their extraction can be performed through recursive approaches assessing normalization quality (Xu et al., 2021), algebraic formulations (Marpu et al., 2011, Nielsen et al., 1998), or by

This contribution has been peer-reviewed. The double-blind peer-review was conducted on the basis of the full paper.
https://doi.org/10.5194/isprs-annals-XI-1-2026-71-2026 | © Author(s) 2026. CC BY 4.0 License.

computing similarity measures between pixels from different sources (Alberga, 2009). PIFs can be detected using several criteria (Nghien et al., 2025), such as land use data and no-change detection techniques. One widely used non-change detection method is the Multivariate Alteration Detection (MAD) (Nielsen et al., 1998), which helps ensure the spatial stability of detected features and removes outliers.

Radiometric normalization can be conducted either across temporal series from the same sensor—evaluating PIFs under various change detection criteria (Wu et al., 2018)—or between sensors of different types (Nghien et al., 2025).

In this work, we propose a semi-empirical approach inspired by the EL method (Smith and Milton, 1999), and compare it against a radiative transfer-based method (Vermote et al., 1997a).

3. Methods

3.1 Data

3.1.1 Data source - information In this paper, we aim at retrieving SR from aerial at-sensor reflectance using satellite-derived SR as references. The aerial datasets were acquired by the French National Institute of Geographic and Forest Information (IGN) using an UltraCam (UC) Eagle Mark3 sensor, with a 60 cm spatial resolution and four spectral bands (commonly blue, green, red and near-infrared), designed to produce ortho-imagery for photogrammetric applications. The satellite dataset was acquired from the Sentinel-2. Spectral bands B2, B3 and B4 (corresponding to the blue, green and red bands) are used in this study, with a spatial resolution of 10 m. The Sentinel-2 Level-2A product provides SR and AOT at a 10 m spatial resolution, with a revisit period of approximately 5 days. Data are provided by the platform THEIA-LAND (Hagolle et al., 2021), with images acquired on June 16th, 23rd and 26th. Images from June 16th and 26th are only used for change detection (Nielsen et al., 1998). The image from June 23rd, acquired at 10:38 UTC, serves as the SR reference data.

The aerial mission campaign took place between June 23rd and 25th, 2023, covering an area of about 500 km^2 in an administrative department of southern France, with 6239 images acquired between 7:19 UTC and 16:50 UTC. The Sentinel-2 images used in this study cover almost the entire aerial campaign. Some aerial images are nearly synchronous with Sentinel-2 acquisitions, while others were acquired at different times, leading to variations in atmospheric conditions and solar geometry. The 10 m AOT data are used only for a baseline method and for evaluation, but are not required for implementing the proposed method.

3.1.2 Satellite SR spectral pre-processing The Spectral Response Functions (SRF) of Sentinel-2 differ from those of the UC sensor bands. A spectral band adjustment was performed using a spectral transfer matrix derived from (Nghien et al., 2025). This allowed estimating the SR of the corresponding UC sensor bands (Blue, Green, and Red) from the three Sentinel-2 bands (B2, B3, and B4).

3.1.3 Aerial pre-processing The aerial images are first resampled to the satellite spatial resolution, and then a cross-calibration method from (Nghien et al., 2025) is performed to convert its pixel values into at-sensor reflectance in the viewing direction. Equation (1) is used as the sensor radiometric model, describing the relationship between the digital number and the at-sensor reflectance.

$$DN_\Lambda = \frac{t}{4N^2} C_\Lambda F_{0,\Lambda} \rho_{z,\Lambda} cos(\theta_s) \tag{1}$$

where DN is the digital number, ρ_z is the at-sensor reflectance, θ_s is the solar zenith angle, F_0 is the extraterrestrial irradiance at the acquisition time, t is the sensor exposure time, N is the f-number, C_Λ is the radiometric calibration coefficient for each aerial spectral band Λ.

This cross-calibration pre-processing uses the satellite Top-Of-Atmosphere reflectance from the Copernicus Sentinel-2 Level-1C product as a reference.

3.2 Baseline Method

First, we propose to use a reference method based on radiative transfer to retrieve the SR. In this paper, we rewrite the 6S method (Vermote et al., 1997a) based on the MAJA method (Hagolle et al., 2017). This method relies on simulating atmospheric parameters using the AOT derived from satellite data. These AOT values are provided for the satellite footprint at its acquisition time. That implies the atmospheric parameters to be ”correct” when aerial and satellite acquisitions are synchronous, and unknown when aerial acquisition is not synchronous.

The analytical expression for aerial at-sensor reflectance as a function of SR, from (Vermote et al., 1997a) , is given by:

$$\begin{aligned} &\rho_z(\theta_s, \theta_v, \phi_s - \phi_v) = \\ &\quad T^{\uparrow}_{g,z}(\theta_v) T^{\downarrow}_{g,z}(\theta_s) \left[\rho_{R+A,z} + T^{\uparrow}_z(\theta_v) T^{\downarrow}_z(\theta_s) \frac{\rho_s}{1 - S\tilde{\rho_s}} \right] \end{aligned} \tag{2}$$

where θ_v correspond to the viewing zenith angle, and ϕ_s and ϕ_v denote the solar and viewing azimuth angles. The quantities $T^{\uparrow}_z$ and $T^{\downarrow}_z$ represent the total upward and downward atmospheric transmittance, while $T^{\uparrow}_{g,z}$ and $T^{\downarrow}_{g,z}$ describe the upward and downward gaseous transmittance. The intrinsic reflectance of the molecular and aerosol layer is denoted by $\rho_{R+A,z}$. The total atmospheric spherical albedo is expressed as S, and $\tilde{\rho_s}$ accounts for contributions from the surrounding SR.

The atmospheric parameters $T^{\downarrow}_g$, $T^{\uparrow}_g$, $T^{\downarrow}$, $T^{\uparrow}$, S and ρ_{R+A} can be simulated at a 1 nm spectral sampling step using the AOT data available at the time of acquisition, with the 6S code (Vermote et al., 1997b) and Py6S tool (Wilson, 2013). As an approximation, all atmospheric parameters P_Λ (*i.e.,* $T^{\downarrow}_g$, $T^{\uparrow}_g$, $T^{\downarrow}$, $T^{\uparrow}$, ρ_{R+A} and S) are first integrated over the satellite spectral response and then converted to the aerial spectral response:

$$P_\Lambda = \frac{\int P(\lambda) f_\Lambda(\lambda) d\lambda}{\int f_\Lambda(\lambda) d\lambda} \tag{3}$$

where $f_\Lambda(\lambda)$ is the SRF of the satellite sensor and Λ the satellite spectral bands. To simplify the notation, we do not write the parameters and reflectance dependence to the spectral integrated interval Λ.

Sentinel-2 metadata provide the AOT spatial variation for the entire satellite images footprint. Thus, we derived the atmospheric parameters for each pixel using 6S. To retrieve the SR,

https://doi.org/10.5194/isprs-annals-XI-1-2026-71-2026

the only remaining unknown is the contribution from the neighboring SR $\tilde{\rho}_s$. Inspired by (Hagolle et al., 2017), we proceed an iterative process to estimate $\tilde{\rho}_s$: At first, we suppose this contribution to be unblurred: $\tilde{\rho}_s = \rho_s$, and calculate for each pixel the SR. At the following iterations, we apply a Gaussian blur on the resulting image to generate a SR with neighbor contribution $\tilde{\rho}_s$ and calculate the SR. We iterate until this estimate of $\tilde{\rho}_s$ converges.

This method removes the atmospheric effect between the airborne sensor and the ground, giving a SR in the viewing direction for Lambertian features under known conditions by applying a radiative transfer code to the at-sensor airborne images.

However, the simulation of the different atmospheric parameters in the radiative transfer code assumes that we dispose of the AOT values for each aerial image at their specific localization and time of acquisition or that the AOT is invariant during the entire acquisition campaign, spatially and temporally.

3.3 Proposed Method - semi-empirical linear correction

In order to overcome the atmospheric variations for the non-ideal case, where aerial images are acquired at a different time or day than the satellite acquisition, and being able to retrieve SRs, we propose a semi-empirical correction method to remove atmospheric effects. In this approach, Sentinel-2 surface reflectance (SR) and aerial at-sensor reflectance over PIFs are used as reference data to establish an affine relationship between ground-level and airborne measurements. This relationship allows us to jointly compensate for atmospheric effects and radiometric calibration differences between the aerial and satellite images.

3.3.1 Hypothesis: EL method First, we simplify Equation (2) by assuming that the total spherical albedo S is zero ($S = 0$) in order to obtain an affine relation between the SR and the at-sensor reflectance. Writing this hypothesis, Equation (2) becomes:

$$\rho_z = T^{\uparrow}_{g,z}(\theta_v) T^{\downarrow}_{g,z}(\theta_s) \left[\rho_{R+A,z} + T^{\uparrow}_{z}(\theta_v) T^{\downarrow}_{z}(\theta_s) \rho_s \right] \tag{4}$$

which can be simplified as:

$$\rho_s = A \cdot \rho_z + B \tag{5}$$

where

$$A = \frac{1}{T^{\uparrow}_{z}(\theta_v) T^{\downarrow}_{z}(\theta_s)} \tag{6}$$

$$B = -\frac{\rho_{R+A,z} T^{\uparrow}_{g,z}(\theta_v) T^{\downarrow}_{g,z}(\theta_s)}{T^{\uparrow}_{z}(\theta_v) T^{\downarrow}_{z}(\theta_s)} \tag{7}$$

However this hypothesis will bring an overestimation error of the SR ρ_s in the atmospheric correction. This error is described as ε in Equation (8):

$$\varepsilon = \frac{1}{1 - S\tilde{\rho}_s} - 1 \tag{8}$$

Using Sentinel-2 Level-2A AOT data, we simulated the total spherical albedo S for each satellite spectral band using the 6S code and determined its minimum and maximum values. For each band, we found the minimum and maximum values of the SR from the Sentinel-2 Level-2A SR data. Then we calculate the potential error using Equation (8).

Table 1 summarizes the potential error resulting from the assumption of zero total spherical albedo for the retrieved SR. These results support the assumption. This approximation introduces an error of approximately 3%, causing an increase in the SR for the worst case scenario.

Bands	$[S_{min}, S_{max}]$	$[\rho_{S,min}, \rho_{S,max}]$	ε
B2	[0.126, 0.169]	[0.016, 0.188]	[0.002, 0.034]
B3	[0.081, 0.131]	[0.034, 0.233]	[0.003, 0.031]
B4	[0.044, 0.096]	[0.023, 0.272]	[0.001, 0.027]

Table 1. Variations in SR estimation error related to total spherical albedo and SR, across all AOT and SR values provided by the Sentinel-2 Level-2A product.

3.3.2 Reference features Equation (5) forms the basis of the EL method, which relies on in-situ ground truth measurements. Ideally, the coefficients (A and B) should be determined using these measurements. In this study, we propose not to use in-situ measurements, but instead to identify elements whose at-sensor reflectance is invariant in aerial images and whose SR is invariant in satellite images. Equation (5) is valid under constant atmospheric conditions; since atmospheric measurements are not available, different coefficients must be determined for groups of aerial images acquired almost simultaneously.

We propose an approach that does not require in-situ measurements to solve the EL and correct for the atmospheric effects. PIFs detection is performed, inspired by (Nghien et al., 2025). Specifically, we adopt their PIF criteria and supplement them with additional criteria to detect PIFs between satellite and aerial imagery.

First, we perform change detection (Nielsen et al., 1998) on multiple satellite images of the area acquired five days apart over spectral bands [B2, B3, B4] to identify elements that are invariant in SR, ensuring the stability of the detected features.

Regarding the invariance of aerial images, we rely on change detection: an edge detector is applied to remove edges and prevent potential misalignment errors. To neglect directional effects, an angular difference mask is applied to the aerial images to select only pixels with viewing conditions similar to those of the satellite images. We add a water area detection to prevent specular reflection.

Applying all these filters can be overly restrictive for many images, depending on the land use. To mitigate this, we group all images acquired within the same 30-second interval into a single patch. For each patch, PIFs are filtered, and atmospheric coefficients (A, B) are estimated from Equation (5) using a RANSAC algorithm. This approach allows the same coefficients to be applied consistently to all images in the patch. The RANSAC algorithm further removes potential outliers among the filtered PIFs by retaining only inliers whose reflectance deviates by no more than 0.01 from the model, ensuring robust coefficient estimation.

Determining PIFs ensure the atmospheric variations caused by temporal variation between aerial and satellite images are compensated by the atmospheric coefficients.

3.4 Evaluation

3.4.1 Experimental design For this study, we focus on 4 different sites covered by both surveys, presenting all cases of the parameters we want to study: synchronous images, non-synchronous images, same atmospheric conditions, and different atmospheric conditions. For each site, we need a significant number of PIFs to ensure robust parameter estimation and the stability of the model. After finding the location corresponding to the studied criteria (synchronous, not synchronous etc), we select images that have same atmospheric conditions (for the 4 locations, select images acquired within the same 30 seconds in the aerial acquisition campaign).

That leads to have between 3 and 6 images for each sites, and represents on average 30 km^2 ($\sim$ 280000 pixels per site). In the covered areas, land use is mainly crop fields, with a few roads and small towns. In any case the PIF selection will eliminate outliers and variant features. Figure 2 presents the locations of the 4 studied sites.

Site 1 corresponds to the 3 images nearly synchronized with the satellite reference image. They are acquired within a 30 seconds interval, at 10:37 UTC. For this studied site, we have AOT values applicable to aerial images, because the atmosphere is similar between satellite and aerial acquisitions. It is the ideal situation for the baseline method, that relies on a radiative transfer code depending on the knowledge of atmospheric optical depth parameter.

Site 2 corresponds to aerial images acquired at 14:15 UTC. This area was chosen because it was the most distant images in time to the satellite image for the same day. Atmosphere is expected to change between the satellite and aerial acquisition, so the baseline method is supposedly not well performing.

Site 3 corresponds to the aerial images acquired at a different day than the reference Sentinel-2 image (June 24th 2023) but with the same solar position as the reference.

Site 4 corresponds to aerial images acquired on a different day and a different solar position, to measure the improvement of the proposed atmospheric correction relative to the baseline method.

All characteristics are summarized in Table 2. We write Δt the time difference in hours between the aerial acquisition and satellite reference image.

	AOT	Δt (hours)	θ_s
Site 1	Known	0	$\theta_{s,aer} = \theta_{s,sat}$
Site 2	Unknown	4	$\theta_{s,aer} \neq \theta_{s,sat}$
Site 3	Unknown	24	$\theta_{s,aer} = \theta_{s,sat}$
Site 4	Unknown	27	$\theta_{s,aer} \neq \theta_{s,sat}$

Table 2. Summary table of all sites characteristics (Δt the time difference in hours between the aerial acquisition and satellite reference image, $\theta_{s,aer}$ and $\theta_{s,sat}$ the solar zenithal angle (SZA) of aerial and satellite images.

Figure 1 shows the Sentinel-2 image coverage (grey) with the locations of the optical centers for aerial photographs (dots) and Figure 3 presents the extracted Pseudo-Invariant Features of the 4 studied locations.

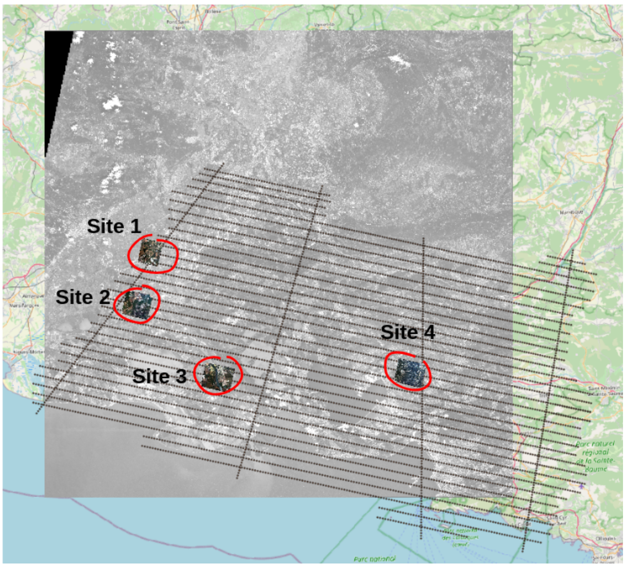

Figure 1. Sentinel-2 footprint and aerial campaign coverage with locations of the four study sites.

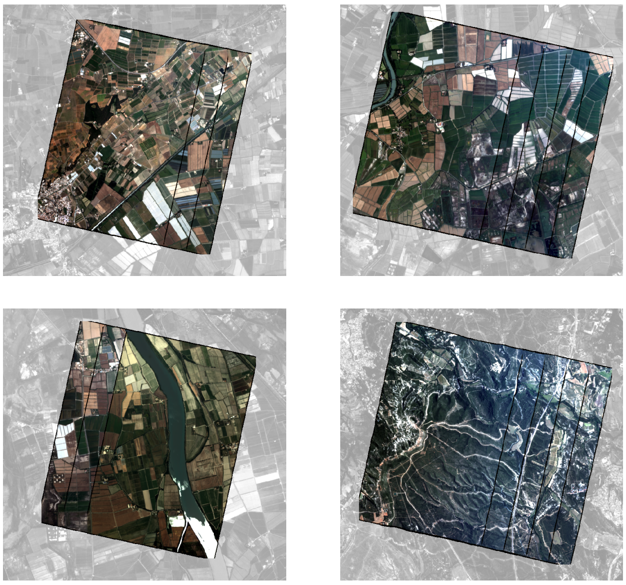

Figure 2. (From left to right and top to bottom) RGB images of the four study sites within the Sentinel-2 footprint. Each aerial image is delimited by a black frame.

The performance of the method is assessed by comparing retrieved SR for PIFs with reference satellite derived SR (Copernicus, Sentinel-2 Level-2A). Indeed, the comparison between methods must be performed only on invariant features to ensure that directional effects remain negligible. The evaluation is based on two metrics computed over the PIFs: the Mean Average Percentage Error (MAPE) and the relative Root Mean Square Error (RMSE) , which ranges between 0 and 1 and is dimensionless. The MAPE and RMSE for the PIFs are defined as:

$$MAPE = \frac{100}{n} \sum_{i=1}^{n} \frac{|\hat{\rho}_{s,i} - \rho_{s,i}|}{\rho_{s,i}} \tag{9}$$

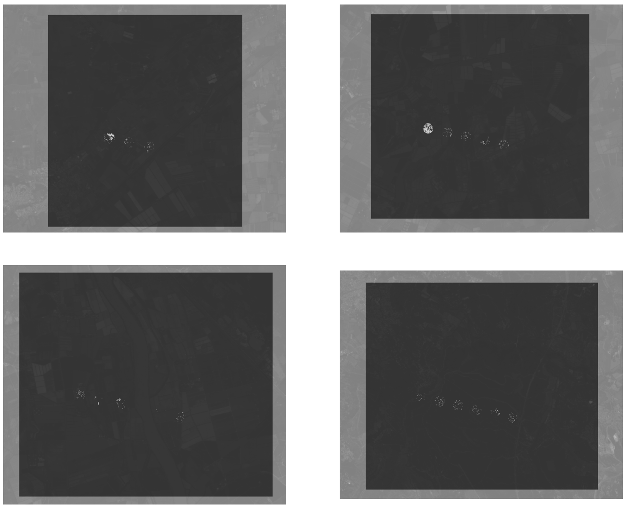

Figure 3. (From left to right and top to bottom) Extracted PIFs of the four studied sites. The sites footprint are in dark gray and the PIFs in white.

$$RMSE = \sqrt{\frac{1}{n}\sum_{i=1}^{n}\frac{(\hat{\rho}_{s,i} - \rho_{s,i})^2}{\rho_{s,i}^2}} \tag{10}$$

The validity of the affine model is evaluated upon 2 criteria: the relative Root Mean Square Error (RMSE) and the determination coefficient (R^2). The coefficient of determination can be expressed as:

$$R^2 = 1 - \frac{\sum_{i=1}^{n}(\hat{\rho}_{s,i} - \rho_{s,i})^2}{\sum_{i=1}^{n}(\bar{\rho_s} - \rho_{s,i})^2} \tag{11}$$

where n is the number of PIF pixels in each site, ρ_s the Level-2A reference reflectance, $\hat{\rho}_{s,i}$ the retrieved reflectance and $\bar{\rho}_{s,i}$ the mean of reference reflectance.

The evaluation is performed on the aerial spectral bands $\Lambda \in$ [B, G, R] at the reference Sentinel-2 spatial resolution (10 m). Both the baseline and proposed methods were applied to the four studied sites (Figure 3), and all metrics were computed using only the inliers filtered by RANSAC from the PIFs. Concerning the baseline method, the AOT values provided by the Sentinel-2 at the moment of satellite acquisition are used to calculate the atmospheric parameters for all sites.

In this study, the retrieved SR for Site 1 is expected to be stable (compared to Level-2A Sentinel-2 product) because of the synchronous time of acquisition between the satellite and the airplane. In this case, the AOT values used to simulate the atmospheric parameters at the airplane acquisition are those provided by Sentinel-2. In contrast, for the other Sites (2, 3, 4), the aerial images are acquired in a non-synchronous situation. That implies that the AOT values may have changed. Consequently, the derived atmospheric parameters may be incorrect.

Indeed, even if the baseline correction takes into account the spatial AOT variation, it is not guaranteed that the AOT is temporally invariant. So, we can expect that, for the majority of aerial images, the atmospheric correction may not be accurate.

4. Results and discussion

4.1 Quantitative evaluation

Figure 4 shows the scatter plot of the reference SR versus aerial at-sensor reflectance for the blue spectral band at Site 2, and Table 3 presents the coefficient of determination values evaluating the affine model’s performance for all sites. These results demonstrate the effectiveness of the proposed linear model.

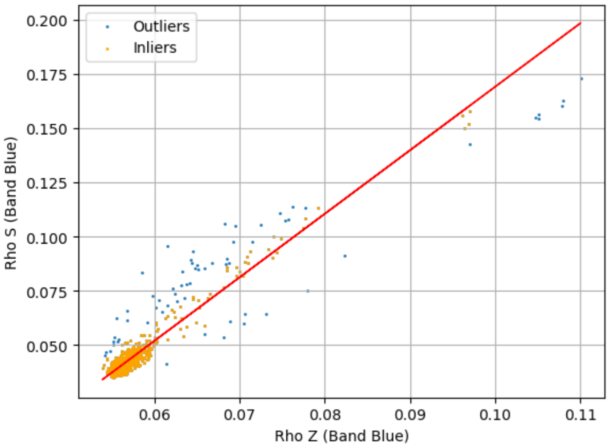

Figure 4. Affine relation between ρ_s and ρ_z for site 2 - Blue spectral band.

All metrics are calculated for these four sites and displayed in Table 4.

Table 3 shows the metrics measuring the validity of the affine model, and Figure 4 shows the affine relation between ρ_S and ρ_z for one patch of images.

Finally, Figures 5 and Figure 6 show the variations of the MAPE and RMSE in the four different sites for both baseline and proposed methods.

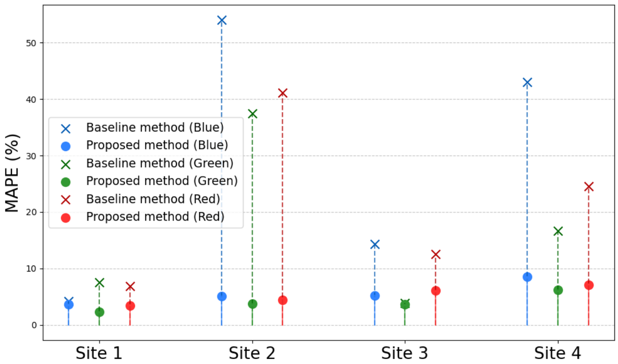

Figure 5. MAPE in % for the 4 studied sites, for each aerial spectral band for both baseline and proposed methods.

For each site, a substantial number of PIFs was extracted (Table 3). The RANSAC algorithm retained between 76.78% and 94.36% of the identified PIFs, effectively removing potential outliers among the extracted elements.

The variability of the errors for Site 1 is first examined. This Site corresponds to aerial images acquired synchronously with the reference satellite image. Consequently, the AOT can be considered invariant, and the values used for the simulation of

Band	$\mathbf{R}^2 \in [0, \mathbf{1}]$				**# PIFs (pixels)**				**% Inliers**			
	Site 1	**Site 2**	**Site 3**	**Site 4**	**Site 1**	**Site 2**	**Site 3**	**Site 4**	**Site 1**	**Site 2**	**Site 3**	**Site 4**
Blue	0.963	0.951	0.935	0.592	247	703	148	221	92.86%	92.99%	87.57%	82.77%
Green	0.976	0.929	0.784	0.713	236	694	142	237	92.48%	92.16%	84.02%	88.76%
Red	0.990	0.965	0.823	0.770	220	675	113	199	82.71%	89.29%	66.86%	74.53%

Table 3. Coefficient of determination R^2, number of PIFs, and percentage of inliers retained by RANSAC, per spectral band and per site.

		MAPE (%)				**RMSE** $\in [\mathbf{0}, 1]$			
Method	**Band**	**Site 1**	**Site 2**	**Site 3**	**Site 4**	**Site 1**	**Site 2**	**Site 3**	**Site 4**
Baseline	Blue	4.224	53.969	14.307	42.957	0.057	0.540	0.150	0.435
	Green	7.534	37.478	3.940	16.619	0.088	0.376	0.050	0.183
	Red	6.843	41.128	12.503	24.509	0.080	0.413	0.128	0.262
Ours	Blue	**3.691**	**5.163**	**5.334**	**8.587**	**0.044**	**0.068**	**0.070**	**0.104**
	Green	**2.326**	**3.774**	**3.674**	**6.208**	**0.034**	**0.047**	**0.044**	**0.077**
	Red	**3.440**	**4.429**	**6.131**	**7.140**	**0.041**	**0.056**	**0.072**	**0.080**

Table 4. MAPE (%) and RMSE $\in [0, 1]$ for aerial spectral bands Blue, Green, and Red across all studied sites, comparing the baseline and proposed methods.

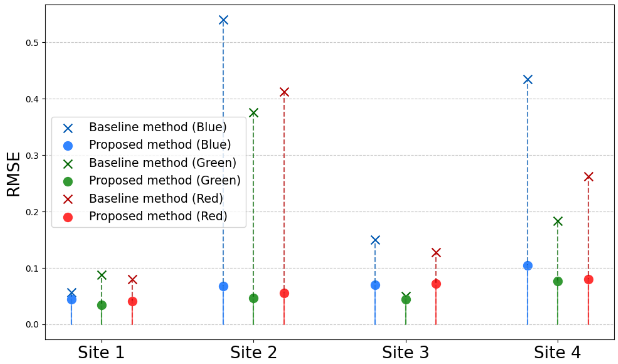

Figure 6. RMSE relative for the 4 studied sites, for each aerial spectral band for both baseline and proposed methods.

atmospheric parameters are assumed to be accurate. This is confirmed by the low error observed for the baseline model. The error obtained with the proposed model is of a similar magnitude, and slightly lower overall. As illustrated in Figure 4, the reference SR is plotted as a function of the at-sensor aerial reflectance. The distinct clusters of points likely correspond to different land cover types.

For Site 2, the error of the baseline model increases notably. This can be explained by temporal atmospheric variability, which propagates through the computation of atmospheric parameters when relying on AOT values acquired several hours earlier. In contrast, the proposed method compensates for this aerosol variation through the adjustment of its coefficients (A_Λ, B_Λ).

Site 3 is characterized by having the same solar zenith angle (θ_s) as the satellite acquisition, despite a 24-hour difference in the aerial acquisition time. Although atmospheric conditions are presumably different, the error from the baseline radiative transfer model is smaller than that observed for Site 2, and for the green spectral band it approaches the error level of the proposed model. This could be explained by the cancellation of directional effects due to the similar solar geometry. The PIF detection step may include some outliers, potentially accounting for the higher error in the proposed model. Additionally, the large temporal gap likely introduces surface variability.

It can be observed that the baseline method shows lower errors for Site 3 and Site 4 compared to Site 2, even though the temporal difference between acquisitions is much larger. This may be explained by atmospheric conditions that happened to be closer to those of the Sentinel-2 acquisition, which could not have been anticipated.

We use the Sentinel-2 SR generated by the MAJA processor as the reference. (Colin et al., 2023) compared MAJA SR with in-situ SR measurements from the ROSAS network. At the La Crau station (located within the study area and close to Site 3), the comparison shows that the RMSE in the visible bands ranges from 0.007 to 0.011. This uncertainty is much smaller than the RMSE obtained between our estimated SR and MAJA SR. This suggests that the RMSE relative to MAJA SR should be close to that relative to in-situ measurements.

4.2 Recomposing coloured images

Although retrieving surface reflectance (SR) through atmospheric correction is primarily intended for quantitative applications in remote sensing, we provide here a qualitative visual assessment of the RGB colour recomposition: a visual comparison between the aerial digital numbers, aerial at-sensor reflectance and ground reflectances (Figure 7).

The original 16-bit aerial digital numbers of all bands were mapped to a common 8-bit display range using a simple linear stretch (Figure 7a). This uniform clipping and rescaling avoids per-band normalization and white-balancing, thereby preserving the inter-band radiometric relationships in the visualization. As a result, the displayed colors reflect the original sensor response rather than being visually balanced.

For the reference Sentinel-2 Level-2A SR image, we generated 16-bit High Dynamic Range (HDR) images that aim to represent the most realistic ground reflectance possible. The same

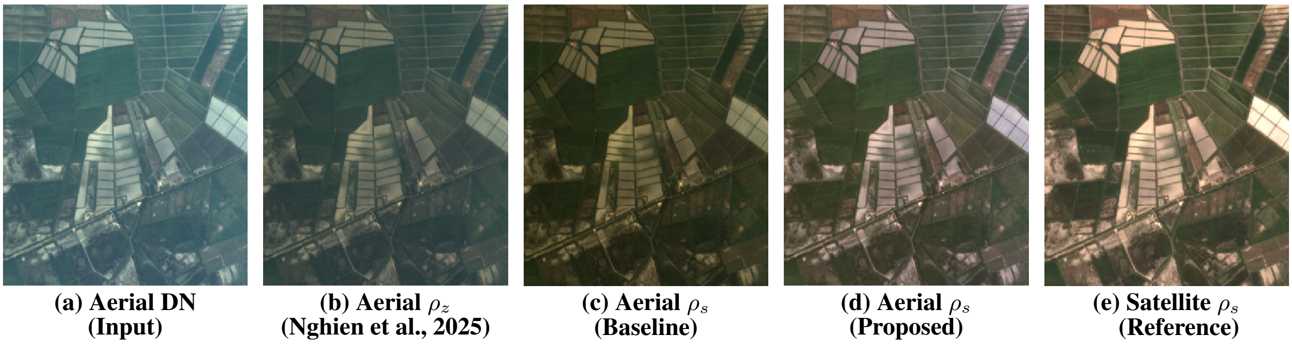
(a) Aerial DN (Input) **(b) Aerial ρ_z (Nghien et al., 2025)** **(c) Aerial ρ_s (Baseline)** **(d) Aerial ρ_s (Proposed)** **(e) Satellite ρ_s (Reference)**

Figure 7. Processing steps from raw aerial images to the reference Sentinel-2 target: (a) Aerial digital numbers - input, (b) At-sensor reflectance, (c) SR from aerial image using the baseline method, (d) SR from aerial image using the proposed method, (e) Sentinel-2 Level-2A - reference target.

tone mapping strategy was applied so that the imagery faithfully reflects the original satellite sensor response (Figure 7e).

We subsequently applied the tone mapping properties of the reference Sentinel-2 Level-2A SR (Figure 7e) image to the retrieved reflectance images : calibrated aerial images (Figure 7b), SR recovered by the baseline (Figure 7c) and proposed methods (Figure 7d). This was done to enable a direct visual comparison of the RGB rendering of the retrieved surface reflectance.

Between the input (Figure 7a) and the target (Figure 7e), the disappearance of an atmospheric bluish haze is clearly observable.

First, moving from an uncalibrated digital number in Figure 7a to a physical quantity of reflectance, sensor calibration effects can be seen in Figure 7b. Then, when removing the atmospheric effect from at-sensor to surface reflectance, most of the atmospheric blue haze is removed (Figures 7c and 7d). The baseline SR image (Figure 7c) appears systematically darker than the Sentinel-2 Level-2A reference, whereas the proposed method produces a brighter result (Figure 7d) that is visually closer to the reference.

However, despite the physically-based processing, the ground reflectance images (Figure 7d and Figure 7e) still do not appear fully realistic. This can be attributed to several factors:

- The absence of white balancing, which maintains radiometric fidelity but produces colors that differ from typical photographic renderings.
- Differences in sensor spectral responses, which limit the perceptual similarity even after spectral conversion.
- The use of a strict linear stretch, which preserves radiometric consistency but may compress perceptually important contrast variations.

These factors can explain why the images may look visually unusual when compared to white-balanced orthophotographs.

The goal of this study, however, is to obtain images in ground reflectance. Physical accuracy takes priority over the realistic appearance of colors which is not the purpose of this study. A color balance could still be applied after the reflectance product has been retrieved.

4.3 Reliability, robustness and spatial limitations

The reliability of the proposed correction method strongly depends on the availability, spatial distribution, and stability of PIFs, which are ensured through the approach described in (Nghien et al., 2025).

Under extreme or highly variable atmospheric conditions, the method remains largely insensitive to temporal atmospheric variations. Provided that the selected ground reference points satisfy the PIF criteria, it can effectively estimate the atmospheric contribution to the signal. However, in the presence of significant spatial variability, a single linear relationship is insufficient to accurately model atmospheric effects over the entire study area. To address this limitation, the estimation of atmospheric contribution is performed locally using a limited set of neighboring aerial images.

5. Conclusion

In this paper, we demonstrated the possibility of correcting atmospheric effects between an airborne sensor and the ground using a semi-empirical method, independently of the need of atmospheric parameters.

Inspired by the EL method, this approach does not require in-situ ground measures to determine the affine parameters but instead uses a PIF approach for which we determine affine parameters to apply to the whole image to remove atmospheric effects.

The proposed method is quantitatively comparable to a radiative transfer model under ideal acquisition conditions (notably when AOT values are available), but shows significantly better results under non-ideal conditions. This method relies primarily on the quality of the determined PIFs, which are crucial for achieving high-quality results. It assumes that the SR provided by a third-party product (in this case, a satellite) serves as a reference.

Further work could focus on improving the selection of PIFs, and potentially using more aerial images to apply the proposed method. Directional effects could then be accounted for, benefiting from the spatial coverage provided by successive aerial images.

References

Alberga, V., 2009. Similarity Measures of Remotely Sensed Multi-Sensor Images for Change Detection Applications. *Remote Sensing*, 1(3), 122–143.

Berra, E. F., Gaulton, R., Barr, S., 2019. Assessing spring phenology of a temperate woodland: A multiscale comparison of ground, unmanned aerial vehicle and Landsat satellite observations. *Remote Sensing of Environment*, 223, 229–242.

Colin, J., Hagolle, O., Landier, L., Coustance, S., Kettig, P., Meygret, A., Osman, J., Vermote, E., 2023. Assessment of the Performance of the Atmospheric Correction Algorithm MAJA for Sentinel-2 Surface Reflectance Estimates. *Remote Sensing*, 15(10), 2665.

Collings, S., Caccetta, P., Campbell, N., Wu, X., 2011. Empirical models for radiometric calibration of digital aerial frame mosaics. *IEEE Transactions on Geoscience and Remote Sensing*, 49(7), 2573–2588.

Elvidge, C. D., Yuan, D., Weerackoon, R. D., .S, L. R., 1995. Relative Radiometric Normalization of Landsat Multispectral Scanner (MSS) Data Using an Automatic Scattergram-Controlled Regression. 1255–1260.

Guo, Y., Senthilnath, J., Wu, W., Zhang, X., Zeng, Z., Huang, H., 2019. Radiometric Calibration for Multispectral Camera of Different Imaging Conditions Mounted on a UAV Platform. *Sustainability*, 11(4), 978.

Hadjimitsis, D. G., Papadavid, G., Agapiou, A., Themistocleous, K., Hadjimitsis, M. G., Retalis, A., Michaelides, S., Chrysoulakis, N., Toulios, L., Clayton, C. R. I., 2010. Atmospheric correction for satellite remotely sensed data intended for agricultural applications: impact on vegetation indices. *Natural Hazards and Earth System Sciences*, 10(1), 89–95.

Hagolle, O., Colin, J., Coustance, S., Kettig, P., d’Angelo, P., Auer, S., Doxani, G., Desjardins, C., 2021. Sentinel-2 surface reflectance products generated by CNES and DLR: methods, validation and applications. *ISPRS Annals of the Photogrammetry, Remote Sensing and Spatial Information Sciences*, V-1-2021, 9–15.

Hagolle, O., Dedieu, G., Mougenot, B., Debaecker, V., Duchemin, B., Meygret, A., 2008. Correction of Aerosol Effects on Multi-Temporal Images Acquired with Constant Viewing Angles: Application to Formosat-2 Images. *Remote Sensing of Environment*, 112(4), 1689–1701.

Hagolle, O., Huc, M., Desjardins, C., Auer, S., Richter, R., 2017. MAJA Algorithm Theoretical Basis Document. Technical Report MAJA-TN-WP2-030 V1.0, Zenodo.

Honkavaara, E., Arbiol, R., Markelin, L., Martinez, L., Cramer, M., Bovet, S., Chandelier, L., Ilves, R., Klonus, S., Marshal, P., Schläpfer, D., Tabor, M., Thom, C., Veje, N., 2009. Digital airborne photogrammetry—a new tool for quantitative remote sensing?—a state-of-the-art review on radiometric aspects of digital photogrammetric images. *Remote Sensing*, 1(3), 577–605.

Jiang, J., Zhang, Q., Wang, W., Wu, Y., Zheng, H., Yao, X., Zhu, Y., Cao, W., Cheng, T., 2022. MACA: A Relative Radiometric Correction Method for Multiflight Unmanned Aerial Vehicle Images Based on Concurrent Satellite Imagery. *IEEE Transactions on Geoscience and Remote Sensing*, 60, 1–14.

Kaufman, Y. J., Sendra, C., 1988. Algorithm for automatic atmospheric corrections to visible and near-IR satellite imagery. *International Journal of Remote Sensing*, 9(8), 1357–1381.

Liang, S., 2005. *Quantitative remote sensing of land surfaces*.

Marpu, P., Gamba, P., Benediktsson, J. A., 2011. Hyperspectral change detection using IR-MAD and feature reduction. *2011 IEEE International Geoscience and Remote Sensing Symposium*, IEEE, Vancouver, BC, Canada, 98–101.

Moghimi, A., Mohammadzadeh, A., Celik, T., Amani, M., 2021. A Novel Radiometric Control Set Sample Selection Strategy for Relative Radiometric Normalization of Multitemporal Satellite Images. *IEEE Transactions on Geoscience and Remote Sensing*, 59(3), 2503–2519.

Nghien, A., Lei, M., Brédif, M., Hagolle, O., 2025. Radiometric Cross-Calibration of an Aerial Sensor with Satellite Top-of-Atmosphere Reflectance. *The International Archives of the Photogrammetry, Remote Sensing and Spatial Information Sciences*, XLVIII-M-7-2025, 49–55.

Nielsen, A. A., Conradsen, K., Simpson, J. J., 1998. Multivariate Alteration Detection (MAD) and MAF Postprocessing in Multispectral, Bitemporal Image Data: New Approaches to Change Detection Studies. *Remote Sensing of Environment*, 64(1), 1–19.

Rahman, H., Dedieu, G., 1994. SMAC: A Simplified Method for the Atmospheric Correction of Satellite Measurements in the Solar Spectrum. *International Journal of Remote Sensing*, 15(1), 123–143.

Rumora, L., Miler, M., Medak, D., 2020. Impact of Various Atmospheric Corrections on Sentinel-2 Land Cover Classification Accuracy Using Machine Learning Classifiers. *ISPRS International Journal of Geo-Information*, 9(4), 277.

Schott, J. R., Salvaggio, C., Volchok, W. J., 1988. Radiometric Scene Normalization Using Pseudoinvariant Features. *Remote Sensing of Environment*, 26(1), 1–16.

Scotford, I., Miller, P., 2005. Applications of Spectral Reflectance Techniques in Northern European Cereal Production: A Review. *Biosystems Engineering*, 90(3), 235–250.

Sharma, A. R., Badarinath, K. V. S., Roy, P. S., 2009. Comparison of Ground Reflectance Measurement with Satellite Derived Atmospherically Corrected Reflectance: A Case Study over Semi-Arid Landscape. *Advances in Space Research*, 43(1), 56–64.

Smith, G. M., Milton, E. J., 1999. The use of the empirical line method to calibrate remotely sensed data to reflectance. *International Journal of Remote Sensing*, 20(13), 2653–2662.

Vermote, E. F., El Saleous, N., Justice, C. O., Kaufman, Y. J., Privette, J. L., Remer, L., Roger, J. C., Tanré, D., 1997a. Atmospheric Correction of Visible to Middle-Infrared EOS-MODIS Data over Land Surfaces: Background, Operational Algorithm and Validation. *Journal of Geophysical Research: Atmospheres*, 102(D14), 17131–17141.

Vermote, E., Tanre, D., Deuze, J., Herman, M., Morcette, J.-J., 1997b. Second Simulation of the Satellite Signal in the Solar Spectrum, 6S: An Overview. *IEEE Transactions on Geoscience and Remote Sensing*, 35(3), 675–686.

Volpi, M., Camps-Valls, G., Tuia, D., 2015. Spectral Alignment of Multi-Temporal Cross-Sensor Images with Automated Kernel Canonical Correlation Analysis. *ISPRS Journal of Photogrammetry and Remote Sensing*, 107, 50–63.

Wilson, R., 2013. Py6S: A Python Interface to the 6S Radiative Transfer Model. *Computers & Geosciences*, 51, 166–171.

Wu, W., Sun, X., Wang, X., Fan, J., Luo, J., Shen, Y., Yang, Y., 2018. A Long Time-Series Radiometric Normalization Method for Landsat Images. *Sensors*, 18(12), 4505.

Xu, H., Wei, Y., Li, X., Zhao, Y., Cheng, Q., 2021. A Novel Automatic Method on Pseudo-Invariant Features Extraction for Enhancing the Relative Radiometric Normalization of High-Resolution Images. *International Journal of Remote Sensing*, 42(16), 6153–6183.

Zhao, W., Tamura, M., Takahashi, H., 2001. Atmospheric and Spectral Corrections for Estimating Surface Albedo from Satellite Data Using 6S Code. *Remote Sensing of Environment*, 76(2), 202–212.